

THE EFFECTS OF IRRADIATION ON HOT JOVIAN ATMOSPHERES: HEAT REDISTRIBUTION AND ENERGY DISSIPATION

ROSALBA PERNA¹, KEVIN HENG^{2,4} & FRÉDÉRIC PONT³

Draft version September 24, 2018

ABSTRACT

Hot Jupiters, due to the proximity to their parent stars, are subjected to a strong irradiating flux which governs their radiative and dynamical properties. We compute a suite of 3D circulation models with dual-band radiative transfer, exploring a relevant range of irradiation temperatures, both with and without temperature inversions. We find that, for irradiation temperatures $T_{\text{irr}} \lesssim 2000$ K, heat redistribution is very efficient, producing comparable day- and night-side fluxes. For $T_{\text{irr}} \approx 2200$ – 2400 K, the redistribution starts to break down, resulting in a high day-night flux contrast. Our simulations indicate that the efficiency of redistribution is primarily governed by the ratio of advective to radiative timescales. Models with temperature inversions display a higher day-night contrast due to the deposition of starlight at higher altitudes, but we find this opacity-driven effect to be secondary compared to the effects of irradiation. The hotspot offset from the substellar point is large when insolation is weak and redistribution is efficient, and decreases as redistribution breaks down. The atmospheric flow can be potentially subjected to the Kelvin-Helmholtz instability (as indicated by the Richardson number) only in the uppermost layers, with a depth that penetrates down to pressures of a few millibars at most. Shocks penetrate deeper, down to several bars in the hottest model. Ohmic dissipation generally occurs down to deeper levels than shock dissipation (to tens of bars), but the penetration depth varies with the atmospheric opacity. The total dissipated Ohmic power increases steeply with the strength of the irradiating flux and the dissipation depth recedes into the atmosphere, favoring radius inflation in the most irradiated objects. A survey of the existing data, as well as the inferences made from them, reveals that our results are broadly consistent with the observational trends.

Subject headings: planets and satellites: atmospheres

1. INTRODUCTION

Hot Jupiters are a class of exoplanets believed to have their rotational period synchronized with their orbital motion due to the strong tidal forces resulting from the proximity to their parent stars. Because of tidal locking, these exoplanets possess permanent day- and night-side hemispheres. These special conditions make hot Jupiters exciting astrophysical laboratories, in which the interplay of radiative forcing, atmospheric dynamics, composition, rotation speed and surface gravity contribute to their observational properties.

A growing body of observations in recent years has allowed for hot Jovian atmospheres to be characterized via a combination of different techniques, which include the measurements of transmission spectra, thermal phase curves, and secondary eclipses. A complex picture has emerged with the objects characterized by a wide range of properties: some display temperature inversions in their atmospheres, others do not; heat redistribution is very efficient in some cases, but highly inefficient in others; a fraction of exoplanets display radii much too large to be compatible with standard evolutionary models.

Theoretical explanations for this variety of phenomena have been abundant. The presence of temperature in-

versions in some exoplanets, but not in others, has been shown to be an effect of atmospheric opacity (Fortney et al. 2008). The variety of recirculation efficiencies, on the other hand, may be attributed to several mechanisms (e.g., Cowan et al. 2012), such as shorter radiative times in hotter exoplanets, stronger magnetic drag (which retards the wind speeds) at higher irradiation fluxes, and a weaker greenhouse with increasing exoplanetary temperature.

For the problem of inflated radii, a variety of possible explanations has been put forward (see, e.g., Fortney & Nettelmann 2010 for a recent review). Bodenheimer et al. (2001) pointed out that tidal dissipation, induced by a non-negligible orbital eccentricity, can pump energy into the interior and hence counteract contraction during evolution. This idea has been further explored and refined by Jackson et al. (2008), Miller et al. (2009) and Ibgui & Burrows (2009). Other ideas (specifically proposed for the case of HD 209458b) include the tidal damping of obliquity (Winn & Holman 2005) and extreme evaporation (Baraffe et al. 2004). Further, it was noted that enhanced opacities in the atmosphere may retard cooling and hence delay contraction (Burrows et al., 2007a, but see also Guillot 2008). Guillot & Showman (2002) have suggested that a fraction of a percent or so of the absorbed stellar flux can be converted into kinetic energy in the deep interior by the breaking of atmospheric waves, but Burkert et al. (2005) were not able to confirm this dissipation mechanism via numerical simulations. More recently, the observation that the flow of ionized particles in the interior generates substantial atmospheric currents

¹ JILA and Department of Astrophysical and Planetary Sciences, University of Colorado, Boulder, CO 80309, U.S.A.

² ETH Zürich, Institute for Astronomy, Wolfgang-Pauli-Strasse 27, CH-8093, Zürich, Switzerland

³ University of Exeter, Stocker Road, Exeter EX4 4QL, U.K.

⁴ Zwicky Prize Fellow

has led to investigations which showed that Ohmic dissipation can inject enough energy in the deep atmospheric levels to affect the evolution of the radius (Batygin & Stevenson 2010; Perna et al 2010b).

Ultimately, discrimination among various models will happen through a close comparison with the data, as more accumulate. From an observational standpoint alone, current data strongly hint at the fact that *the strength of the irradiating flux* plays a major role in determining the degree of heat redistribution (Harrington 2011), as well as the amount of radius inflation (e.g., Fortney et al. 2010). This is unsurprising, since irradiation is the main energy provider in these exoplanets. However, from a theoretical point of view, the direct link between strength of irradiation and those fundamental observational properties of the exoplanets has not been elucidated yet. This has motivated our current work.

In this paper, by means of global, 3D atmospheric circulation models with dual-band radiative transfer tailored to hot Jupiters (Heng, Frierson & Phillipps 2011), we explore, as a function of the irradiating flux from the parent star:

- a) The efficiency of heat redistribution from day to night side, focusing on the infrared photosphere, and the relative day-night brightness contrast;
- b) The offset of the hotspot (hottest infrared region of the exoplanet) with respect to the substellar point;
- c) The magnitude of hydrodynamic dissipation due to both the onset of the Kelvin-Helmholtz instability and shocks;
- d) The strength of Ohmic dissipation.

We present a suite of 16 models: for eight values of the irradiation temperature (spanning the range $T_{\text{irr}} \approx 770 - 3000$ K), and each for cases with and without a temperature inversion.

Our simulations allow us to elucidate the relative importance of irradiation and opacity (correlated with temperature inversions) in determining the observational properties of the exoplanet. They also allow us to assess what is the main effect in determining heat redistribution and day-night contrast, and to predict theoretically, for the first time, the temperature or irradiating flux around which redistribution begins to break down. Furthermore, by computing the Richardson number and the Mach number at each point in the flow, we can quantitatively estimate the depth down to which the flow can be subject to either shear instabilities or shocks, and hence whether hydrodynamic dissipation of this type can affect radius inflation. Similarly, our simulations allow us to follow the depth down to which Ohmic power can be dissipated, as a function of the irradiation strength, and for models with varying opacities.

Our paper is organized as follows: in §2, we summarize the main features of our simulations, and provide the specific details for the models that we study. Our results for heat redistribution and the hotspot location are presented in §3, while in §4 we study hydrodynamic and Ohmic dissipation. A qualitative comparison with observations is made in §5. We finally summarize and conclude in §6. For completeness, we provide zonal-mean profiles of the zonal wind, temperature, potential temperature and streamfunction in Appendix A.

2. METHODOLOGY

Our 3D atmospheric circulation models are based on the computational setup described in Heng, Menou & Phillipps (2011) and Heng, Frierson & Phillipps (2011). In the following, we summarize its main features, as well as the set of parameters which we use for the current simulations.

2.1. Stellar and orbital parameters

A concise list of the parameters and their adopted values are described in Table 1. Most of the parameters are chosen to have typical values, e.g., the surface gravity of the hot Jupiter is $g_p = 10 \text{ m s}^{-2}$. Since our primary interest is to explore the dependence of selected exoplanetary properties on the strength of irradiation and the shortwave atmospheric opacity, we keep the rest of the parameter values to be the same for all of the models (Table 1).

Assuming a Bond albedo of zero, the irradiation⁵ temperature is defined as (Heng et al. 2012)

$$T_{\text{irr}} = T_{\star} \left(\frac{R_{\star}}{a} \right)^{1/2}, \quad (1)$$

such that the irradiating flux is $\mathcal{F}_0 = \sigma_{\text{SB}} T_{\text{irr}}^4$. (For parameter values appropriate to Earth, one recovers $\mathcal{F}_0 \approx 1370 \text{ W m}^{-2}$, the solar constant.) The irradiating flux \mathcal{F}_0 , stellar radii R_{\star} , effective stellar temperature T_{\star} and exoplanet-star spatial separation a are related by the expression,

$$a = R_{\star} T_{\star}^2 \left(\frac{\sigma_{\text{SB}}}{\mathcal{F}_0} \right)^{1/2} \approx 0.09 \text{ AU} \left(\frac{R_{\star}}{R_{\odot}} \right) \times \left(\frac{T_{\star}}{6000 \text{ K}} \right)^2 \left(\frac{\mathcal{F}_0}{2 \times 10^8 \text{ erg cm}^{-2} \text{ s}^{-1}} \right)^{-1/2}, \quad (2)$$

where σ_{SB} is the Stefan-Boltzmann constant and we have assumed that the exoplanet orbits a Sun-like star. The use of the irradiation, rather than the equilibrium temperature, circumvents the issue of dealing with (confusing) factors of order unity related to assumptions about the efficiency of heat redistribution.

The tidal locking time is (Goldreich & Soter 1966; Bodenheimer et al. 2001)

$$t_{\text{lock}} \approx \frac{8Q}{45\Omega_p} \left(\frac{\omega_p}{\Omega_p} \right) \left(\frac{M_p}{M_{\star}} \right) \left(\frac{a}{R_p} \right)^3, \quad (3)$$

where ω_p and Ω_p are the rotational and orbital frequencies of the exoplanet, respectively. For our models, we get $t_{\text{lock}} \sim 10^3 - 10^8 \text{ yr}$ ($Q/10^6$)(ω_p/Ω_p). Thus, for a Gyr-old solar-like star (which is what we assume), our assumption of tidal locking is plausible and self-consistent if $\omega_p/\Omega_p \sim 1$. If $\omega_p/\Omega_p \sim 10$, then this assumption becomes suspect only for Model C. With the rotational and orbital frequencies being equal, we obtain

$$\Omega_p \approx \left(\frac{GM_{\star}}{a^3} \right)^{1/2}, \quad (4)$$

where G is the gravitational constant and M_{\star} is the stellar mass. Thus, \mathcal{F}_0 , Ω_p and a need to be varied self-

⁵ In this study, we use the terms ‘‘irradiation’’ and ‘‘isolation’’ interchangeably.

TABLE 1
TABLE OF COMMON PARAMETERS AND THEIR VALUES

Symbol	Description	Units	Value(s)
τ_{S_0}	normalization for optical depth of shortwave absorbers	—	$5 \times 10^3, 5 \times 10^4$
τ_{L_0}	normalization for optical depth of longwave absorbers	—	10^4
ϵ	enhancement factor due to collision-induced absorption	—	1
c_P	specific heat capacity at constant pressure (of the atmosphere)	$\text{J K}^{-1} \text{kg}^{-1}$	14550.4
\mathcal{R}	specific gas constant (of the atmosphere)	$\text{J K}^{-1} \text{kg}^{-1}$	4157.25
$\kappa \equiv \mathcal{R}/c_P$	adiabatic coefficient [†]	$\text{J K}^{-1} \text{kg}^{-1}$	2/7
P_0	reference pressure at bottom of simulation domain	bar	1000
g_p	acceleration due to gravity	m s^{-2}	10
R_p	radius of hot Jupiter	km	7.1×10^4
t_ν	hyperviscous time	day [†]	10^{-6}
N_ν	vertical resolution	—	36

[†]: expressed in terms of an exoplanetary day (i.e., rotational period).

[‡]: we term κ the “adiabatic coefficient”, following Pierrehumbert (2010), and avoid calling it the “adiabatic index” in order to not confuse it with the ratio of specific heat capacities.

consistently. We note that setting the rotational and orbital frequencies to be equal results in a more constrained problem for our simulations. While the existence of close-in, non-spin-synchronized gas giants remains possible, there is little empirical evidence currently available to support such a modelling effort.

We present 16 models in this paper, divided into subgroups which we term “cold” (C, C1 and C2), “warm” (W, W1 and W2) and “hot” (H, H1). For Model W, the irradiating flux \mathcal{F}_0 is chosen to match the threshold value found by Demory & Seager (2011), below which transiting *Kepler* giant exoplanet candidates appear to have non-inflated radii. Each of these models is studied both with and without the presence of a temperature inversion. The parameters specific to each model are reported in Table 2.

2.2. Thermodynamics

The adiabatic coefficient κ is related to the thermodynamical properties of the atmospheric gas (Pierrehumbert 2010),

$$\kappa \equiv \frac{\mathcal{R}}{c_P} = \frac{2}{2 + n_{\text{dof}}}. \quad (5)$$

By assuming the atmosphere to be dominated by molecular hydrogen (i.e., the number of degrees of freedom of the gas is $n_{\text{dof}} = 5$), we get $\kappa = 2/7$. Furthermore, the specific gas constant is related to the mean molecular weight μ and the universal gas constant \mathcal{R}^* by $\mathcal{R} = \mathcal{R}^*/\mu = 4157.25 \text{ J K}^{-1} \text{ kg}^{-1}$. We use $\mu = 2$ to emphasize the detachment from any specific case study, and remark that our results are rather insensitive to small changes in the mean molecular weight (e.g., $\mu = 2.35$ as is typical for a solar mix). It follows that the specific heat at constant pressure is $c_P = 14550.4 \text{ J K}^{-1} \text{ kg}^{-1}$. We recall that the adiabatic index is $\gamma = 1 + 2/n_{\text{dof}} = 7/5$ for an atmosphere dominated by molecular hydrogen and that the sound speed is $c_s = \sqrt{\gamma k_B T / 2m_H}$ with k_B denoting the Boltzmann constant, T the temperature and m_H the mass of a hydrogen atom.

2.3. Atmospheric opacities

In this work, we adopt the dual-band approximation for radiative transfer, namely that the blackbody peaks of the stellar and exoplanetary emission are well separated in wavelength or frequency (see

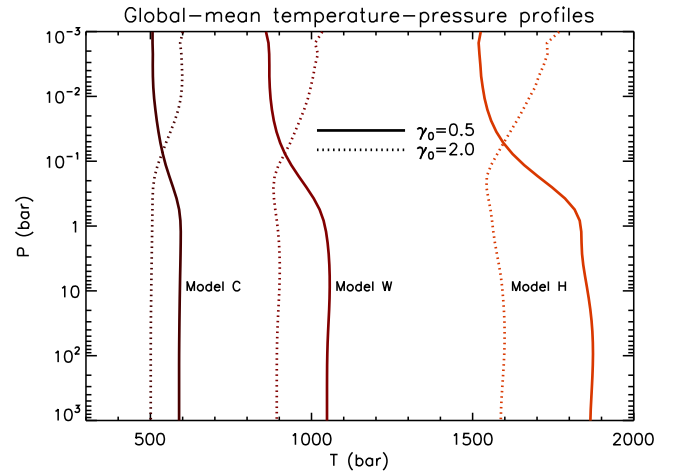


FIG. 1.— The global-mean temperature-pressure profiles for Models C, W and H. Models with $\gamma_0 < 1$ do not display temperature inversions, while models with $\gamma_0 > 1$ do.

Heng, Frierson & Phillipps 2011 and references therein). One then requires two broadband opacities to completely describe the radiative transfer: a shortwave/optical opacity κ_S to quantify the absorption of starlight with depth/pressure and a longwave/infrared opacity κ_L to quantify the absorption of thermal emission from the exoplanet. We neglect the effects of scattering (see Heng 2012). Varying κ_S , while holding κ_L fixed, mimics the effect of extra, shortwave absorbers in the atmosphere, of unspecified chemistry, which cause a temperature inversion when $\kappa_S > \kappa_L$ (Hubeny, Burrows, & Sudarsky 2003, Burrows et al. 2007b, Burrows & Orton 2010, Knutson et al. 2008).

In the absence of empirical constraints, we assume the shortwave opacity to be constant, which means that it is related to the shortwave optical depth in a simple manner,

$$\tau_S = \frac{\kappa_S P}{g_p} = \frac{\tau_{S_0} P}{P_0}, \quad (6)$$

where $P_0 = 1 \text{ kbar}$ is the reference pressure at the bottom of the simulation domain. The longwave optical depth is described by two terms (Heng, Frierson & Phillipps 2011),

$$\tau_L = \tau_{L_0} \left[\frac{P}{P_0} + (\epsilon - 1) \left(\frac{P}{P_0} \right)^2 \right], \quad (7)$$

TABLE 2
TABLE OF PARAMETERS, AND THEIR VALUES, SPECIFIC TO EACH MODEL

Model	\mathcal{F}_0 (W m^{-2})	Ω_p (s^{-1})	a (AU)	T_{init} (K)	Δt (s)	Simulation time (Earth days)	C_{int} ($\text{J K}^{-1} \text{m}^{-1}$)	t_v^{-1} (s^{-1})
C	2×10^4	1.3×10^{-6}	0.28	589, 501	600	4500	10^7	2.1×10^{-1}
C1	5×10^4	2.6×10^{-6}	0.17	741, 630	240	3000	10^7	4.1×10^{-1}
C2	7×10^4	3.4×10^{-6}	0.15	806, 686	240	3000	10^7	5.4×10^{-1}
W	2×10^5	7.5×10^{-6}	0.09	1048, 892	180	2000	10^6	1.2
W1	5×10^5	1.5×10^{-5}	0.06	1317, 1121	120	1500	10^6	2.4
W2	7×10^5	1.9×10^{-5}	0.05	1433, 1219	120	1500	10^6	3.0
H	2×10^6	4.2×10^{-5}	0.03	1863, 1585	120	1500	10^6	6.7
H1	5×10^6	8.4×10^{-5}	0.02	2343, 1994	80	1000	10^6	13.3

Note: initial temperatures quoted are for $\gamma_0 = 0.5$ and 2.0, respectively.

where the second term is an approximate way to account for the effects of collision-induced absorption, which introduces an enhancement factor of ϵ at the bottom of the simulation domain. The longwave optical depth normalization is $\tau_{L_0} = \kappa_0 P_0 / g_p$, where κ_0 is the longwave opacity normalization. We pick $\epsilon = 1$. Ignoring collision-induced absorption in the infrared is a good approximation as long as this effect is only significant at atmospheric layers residing below the longwave photosphere (Heng, Frierson & Phillipps 2011).

In the absence of clouds/hazes, the ratio $\gamma_0 \equiv \kappa_S / \kappa_0$ determines if a temperature inversion exists in the atmosphere (Hubeny, Burrows, & Sudarsky 2003; see also discussion in Heng et al. 2012). If $\gamma_0 > 1$, the shortwave photosphere sits above the longwave photosphere, and an inversion exists; if $\gamma_0 < 1$, the relative locations of the two photospheres are reversed, and there is no inversion. To study the effect of a temperature inversion on the day-night heat redistribution, we examine models with $\gamma_0 = 0.5$ and 2. We choose a typical value for the longwave opacity normalization: $\kappa_0 = 0.01 \text{ cm}^2 \text{ g}^{-1}$ such that the longwave/infrared photosphere resides at

$$P_{\text{IR}} \sim \frac{g_p}{\kappa_0} = 0.1 \text{ bar.} \quad (8)$$

The shortwave opacity follows from the chosen value of γ_0 .

The global-mean temperature-pressure profiles are showed in Fig. 1, for the two chosen values of $\gamma_0 = 0.5$ and 2, and the three representative flux strengths indicated with models C, W, H in Table 2. The effect of the temperature inversion is clearly evident: models with $\gamma_0 = 0.5$ are hotter in the interior, and cooler in the outerparts, while models with $\gamma_0 = 2$ display the opposite behaviour. We have set the internal heat flux of our hot Jupiter models to be zero. For completeness, we include in Appendix A the zonal-mean zonal wind, temperature, potential temperature and streamfunction profiles corresponding to these 6 models.

2.4. Atmospheric dynamics

The Princeton-GFDL FMS dynamical core solves the primitive equations of meteorology (see Heng, Menou & Phillipps 2011 and references therein). In the vertical, we choose the simulation domain to span 6 orders of magnitude in pressure, from $P = 1$ mbar to 1 kbar; the latter value is chosen to roughly match the transition from the radiative to the convective zone of a hot Jupiter. The vertical resolution is $N_v = 36$, such that each pressure scale height is covered by about 3 grid points. The horizontal resolution is

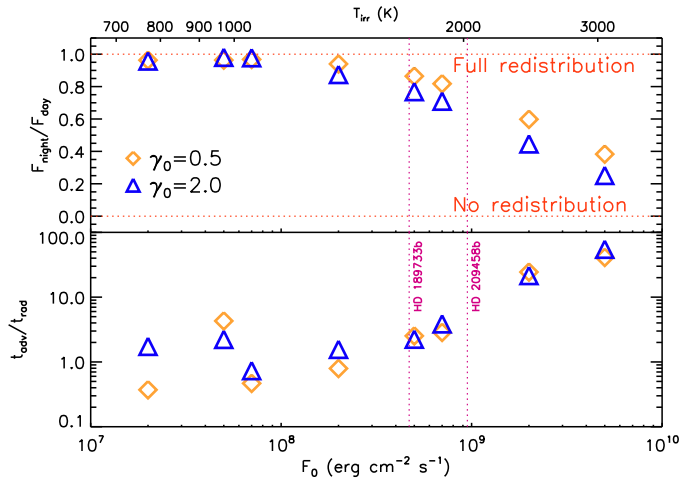


FIG. 2.— *Top*: Ratio of night- to day-side hemispheric, infrared fluxes, for models with various degrees of irradiation. The night-day contrast decreases with T_{irr} , indicating a weakening of the heat redistribution with increasing irradiating fluxes. Models with temperature inversions display a larger flux contrast, but this is a secondary effect compared to the irradiating flux. *Bottom*: Ratios between the advective and the radiative timescale, for the models of the top panel. Redistribution begins to break down when the advective timescale becomes much larger than the radiative time.

192×96 (longitude versus latitude). In the absence of a physically-motivated scheme for more sophisticated initial conditions, the simulations are started from a state of rest with a constant temperature T_{init} .⁶ For $\epsilon = 1$, the initial temperature is (Heng, Frierson & Phillipps 2011)

$$T_{\text{init}} \approx \left[\frac{\mathcal{F}_0}{16\sigma_{\text{SB}}} \left(2 + \frac{\sqrt{3}}{\gamma_0} \right) \right]^{1/4}. \quad (9)$$

The specific value of T_{init} used to initiate each of the models is reported in Table 2.

The areal heat capacity of the simulation bottom (C_{int}) is chosen to have a value such that the thermal inertia of gaseous hydrogen matches the radiative time constant at $P = 1$ kbar (Heng, Frierson & Phillipps 2011). For Models C, W and H, it suffices to adopt $C_{\text{int}} = 10^7, 10^6$ and $10^6 \text{ J K}^{-1} \text{ m}^{-2}$, respectively, as it has been shown by Heng, Frierson & Phillipps (2011) that order-of-magnitude variations in C_{int} produce small ($< 1 \text{ K}$) variations in the temperature-pressure profile.

As already noted by Heng, Menou & Phillipps (2011),

⁶ This particular initial condition is inconsequential for our simulations, since the isothermal initial condition in the code reproduces the radiative solution (Heng, Frierson & Phillipps 2011).

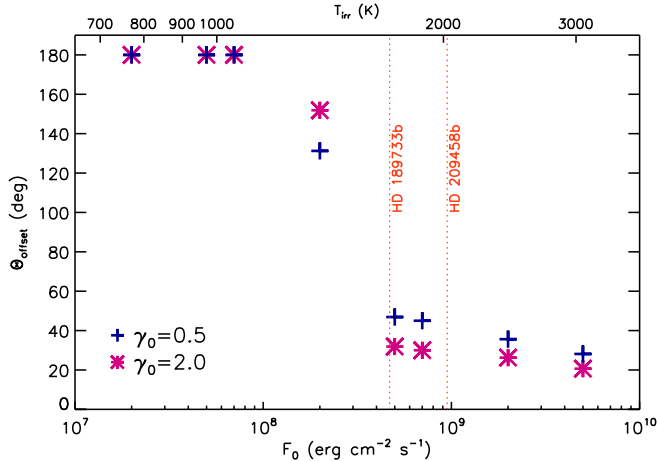


FIG. 3.— Longitudinal separation between the location of the brightest spot on the exoplanet and the substellar point, i.e., the hotspot offset. Note that in the coldest models, the day-night contrast is negligible, and the location of the brightest spot is subject to statistical fluctuations with time. When these conditions occur, we set the offset equal to 180° .

numerical noise accumulates at the grid scale and has to be dissipated via a “hyperviscosity” in our spectral code. Since the hyperviscous term is neither an original nor a physical part of the primitive equations, its value cannot be specified from first principles. As in Heng, Menou & Phillipps (2011) and Heng, Frierson & Phillipps (2011), we pick the order-of-magnitude value of the hyperviscous timescale to be as large as possible in order for the simulations to collectively run to completion: $t_\nu = 2\pi \times 10^{-6}/\Omega_p$. Decreasing the hyperviscous timescale — and hence *increasing* the rate of dissipation (t_ν^{-1}) — by one to two orders of magnitude leaves the hotspot offset largely unchanged (see Fig. 19 of Heng, Frierson & Phillipps 2011), but decreases the zonal wind speeds by $\sim 10\%$ (Heng, Menou & Phillipps 2011). Our estimates for the zonal wind speeds are thus upper limits with regards to this numerical issue.

Finally, we note that convective adjustment is applied when the dry lapse rate becomes super-adiabatic, i.e., the Schwarzschild criterion for convective stability is violated. Our convective adjustment scheme is described in Heng, Frierson & Phillipps (2011).

3. ATMOSPHERIC CIRCULATION, HEAT REDISTRIBUTION, AND HOTSPOT LOCATION

In a strongly irradiated exoplanet, the atmospheric dynamics and radiation are regulated by the interplay of zonal winds, which tend to redistribute/transport heat to cooler regions of the exoplanet, and local re-radiation of the absorbed energy, which favors the emission of radiation at the same location where it was absorbed. The relative efficiency of these two processes can be estimated by means of the associated timescales:

$$t_{\text{adv}} \sim \frac{R}{\max\{v_\Theta\}}, \quad (10)$$

represents the fastest timescale on which zonal winds redistribute temperature variations over the scale of the exoplanet, while the radiative timescale (Goody & Yung

1989)

$$t_{\text{rad}} \sim \frac{c_P P}{\sigma_{\text{SB}} g_p T_{\text{max}}^3} \quad (11)$$

is the characteristic timescale on which thermal energy is radiated away by a parcel of fluid. The latter is given by the ratio of the thermal heat content ($c_P T_{\text{max}} \tilde{m}$ where $\tilde{m} = P/g_p$ is the column mass in hydrostatic equilibrium) to the re-emitted flux ($\sigma_{\text{SB}} T_{\text{max}}^4$). Note that $T_{\text{max}} \equiv T(\max\{v_\Theta\})$. In other words, both timescales are evaluated at the location where the zonal velocity attains its maximum value. Equation (11) is valid at optical depths close to or greater than unity; more precise versions of it carry an order of unity correction factor related to the efficiency of heat redistribution.

Hot Jovian atmospheres possess radiative timescales which vary across many orders of magnitude. At the top of the atmosphere (~ 1 mbar), the atmosphere is radiative ($t_{\text{rad}} \ll t_{\text{adv}}$); at the bottom (~ 1 kbar), it is advective ($t_{\text{rad}} \gg t_{\text{adv}}$). The shortwave opacity controls the height/depth at which the bulk of the starlight is deposited. If the deposition occurs mostly near the top of the atmosphere (high κ_S), then the hotspot offset is small. Conversely, if it occurs near the bottom, then the offset is large. Thus, there is a degeneracy of the hotspot offset on irradiation and optical opacity.

We denote the flux emerging from the longwave photosphere by \mathcal{F}_{OLR} (where “OLR” denotes the “outgoing longwave radiation”, a term commonly used in the atmospheric/climate science community). Denoting the latitude by Φ , its latitudinal average is (Cowan & Agol 2008)

$$\langle \mathcal{F}_{\text{OLR}} \rangle \equiv \frac{1}{\pi} \int_{-\pi/2}^{\pi/2} \mathcal{F}_{\text{OLR}} \cos^2 \Phi \, d\Phi. \quad (12)$$

With the longitude denoted by Θ , the total flux from each hemisphere of the exoplanet is defined as

$$\mathcal{F}_{\text{day,night}} = \frac{1}{\pi} \int_{\Theta_{\text{min}}}^{\Theta_{\text{max}}} \langle \mathcal{F}_{\text{OLR}} \rangle \, d\Theta, \quad (13)$$

where $\{\Theta_{\text{min}}, \Theta_{\text{max}}\} = \{\pi/2, 3\pi/2\}$ for the day side. The night side is described by $\{\Theta_{\text{min}}, \Theta_{\text{max}}\} = \{0, \pi/2\}$ and $\{3\pi/2, 2\pi\}$. The substellar point is set at $\Theta = \pi$. In computing the day-night flux contrast, we have chosen to deal entirely with the latitudinally-averaged OLR or 1D “brightness map”, rather than the thermal phase curve which is a convolution of the physical distribution of flux across longitude and its geometric projection to the observer (Cowan & Agol 2008). Additionally, we choose to plot the ratio of night-to-day fluxes, rather than the more familiar day-to-night ratio, since this is a quantity which ranges between 0 and 1 (rather than between 1 and infinity). However, our discussion will be mostly in the context of day-to-night flux ratios, which we generally refer to as the “day-night contrast”.

Figure 2 shows the day-night contrast for the 16 reference models that we have studied. The three coldest models C, C1 and C2 display a near perfect redistribution of the heating, with comparable day and night fluxes. A slight contrast starts to appear for the W model (irradiated by $\mathcal{F}_0 = 2 \times 10^8 \text{ erg cm}^{-2} \text{ s}^{-1}$), and it then gradually increases with the strength of the irradiating flux. For

the same value of \mathcal{F}_0 , models with temperature inversions display a larger day-night flux contrast since the bulk of the starlight is deposited higher up in the atmosphere where the flow is dominated by radiative cooling rather than advection. The dependence of the flux contrast on opacity (and hence on the presence or not of temperature inversions) is consistent with the results of Fortney et al. (2008) using 1D models (see also Dobbs-Dixon & Lin 2008).

The bottom panel of Fig. 2 shows the ratio between the advective and the radiative timescales as previously defined, for each of the models of the upper panel. Recall that, since flow velocities vary with latitude, and so do the physical distances traveled by the flow from one side to the other of the exoplanet, the advective time is a function of Φ . To assign a unique value in Fig. 2, we searched for the latitude at which the zonal flow attains its maximum speed, and computed the timescales at that latitude. For the coldest cases, the advective and the radiative times are within an order of magnitude of each other. The fluctuations in $t_{\text{adv}}/t_{\text{rad}}$ arise from the fact that the difference between T_{max} and the mean temperature of the flow becomes less pronounced as the strength of irradiation decreases. In other words, describing whether the zonal flow is predominantly advective or radiative by a single number becomes a less robust exercise when the flow becomes more zonally symmetric. Instead, the day-night flux contrast is a better indicator.

As the irradiating flux becomes more intense, the ratio $t_{\text{adv}}/t_{\text{rad}}$ rapidly increases. Our numerical results hence support the qualitative expectation that it is the relative magnitude of these two timescales which mainly determines the extent of heat redistribution, and consequently the day-night flux contrast (Showman & Guillot 2002). We note that, while our study has focused on spin-synchronized planets, the qualitative considerations derived above are expected to hold more generally. A change in the planet spin for the same T_{irr} would modify the flow dynamics (and hence both t_{rad} and t_{adv}); however, the extent to which the flow is able to redistribute heat versus dissipate it locally, would still depend on the relative magnitude of these timescales, as long as the spin period is not much smaller than t_{rad} (in which case the planet would be kept at a uniform temperature).

The longitudinal offset Θ_{offset} between the hotspot location and the substellar point is displayed in Fig. 3. For the three coldest models, the temperature is virtually homogeneous on the entire exoplanet, but is subjected to statistical fluctuations; hence the location of the hottest spot is not well-defined. For these cases, we set $\Theta_{\text{offset}} = 180^\circ$. As the day-night contrast starts to deviate from unity, the hotspot location becomes well-defined. In the W model, the hotspot offset from the substellar point is rather large, $\Theta_{\text{offset}} \approx 130^\circ\text{--}150^\circ$; this is indicative of efficient heat redistribution. As the irradiating flux increases, the hotspot location moves towards the substellar point. This can be easily understood in light of the changing ratio between the advective and the radiative timescales. As advection becomes less effective in keeping up with the rapid cooling of the gas, the hotspot location moves closer to the point of maximum irradiation, i.e., the substellar point.

We note that the effects of opacity and mean molecu-

lar weight were explored by Menou (2012a) using also an atmospheric circulation code with dual-band radiative transfer (Rauscher & Menou 2012), albeit in the context of Neptune-like exoplanets. Our results are qualitatively consistent with those reported in Menou (2012a), where it was found that variations in the shortwave opacity produce non-negligible differences in the hotspot offset. Other studies of the role of atmospheric opacity in controlling the day/night contrast and dynamics have been performed by Lewis et al. (2010), tailored to the hot Neptune GJ436b. Their simulations particularly illustrated the important role of metallicity in regulating atmospheric circulation for a broad range of warm extra-solar planets.

4. DISSIPATION WITHIN THE ATMOSPHERIC FLOW

In this section, we use the 16 models previously described to investigate the importance of various forms of dissipation within the flow, and their relative trends with the strength of the irradiating flux. In particular, we first estimate the contribution to hydrodynamic dissipation from gas which is either Kelvin-Helmholtz unstable and/or shocked, and then we study the additional contribution from Ohmic dissipation if the flow is magnetized.

We remark that, since our simulations do not self-consistently account for the feedback effect of shocks, instabilities, and magnetic drag (all contributing to reducing wind speeds and hence the amount of dissipation), the estimates made in this section should be considered as upper limits for each particular combination of parameters. However, the trends that we find, while likely to be less steep with the presence of feedback effects, are expected to be robust with respect to the dependence on irradiation.

4.1. Hydrodynamic dissipation

Our 3D circulation models, while not directly simulating the onset and development of shocks and shear instabilities, allow us to establish whether the flow is subject to such instabilities and to shocks and to determine the size of the affected region. In the current study, we are primarily interested in exploring the effects of irradiation, while also examining the influence of (shortwave) opacity.

4.1.1. Dissipation from Kelvin-Helmholtz-unstable gas

The first form of hydrodynamic dissipation that we consider is due to the Kelvin-Helmholtz (KH) instability in the thermally-stratified shear flow. Whether such a flow becomes unstable can be estimated by measurements of the Richardson number

$$\mathcal{Ri} = N^2 \left(\frac{\partial v_\Theta}{\partial z} \right)^{-2} = -\mathcal{R}\sigma_0^{\kappa-1} \frac{\partial \theta_T}{\partial \sigma_0} \left(\frac{\partial v_\Theta}{\partial \sigma_0} \right)^{-2}, \quad (14)$$

where

$$N = \left(\frac{g_p}{\theta_T} \frac{\partial \theta_T}{\partial z} \right)^{1/2} \quad (15)$$

is the Brunt-Väisälä frequency, $\theta_T \equiv T(P/P_0)^{-\kappa}$ is the potential temperature, and $\sigma_0 \equiv P/P_0$. The criterion for the flow to become Kelvin-Helmholtz unstable is expressed by the condition $\mathcal{Ri} < 1/4$ (Kundu & Cohen 2004; Li & Goodman 2010).

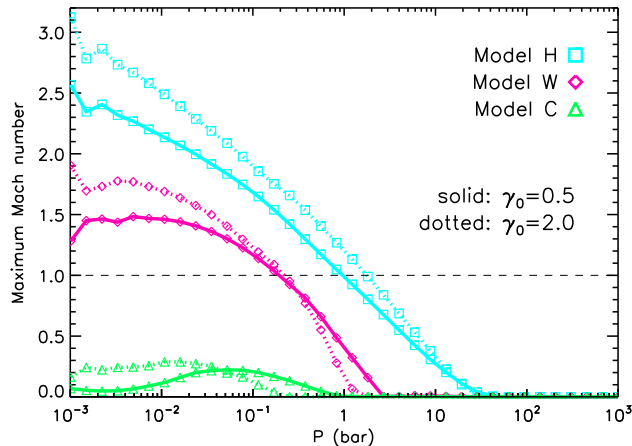


FIG. 4.— Maximum Mach number as a function of depth within the atmosphere, for models with varying degrees of irradiation.

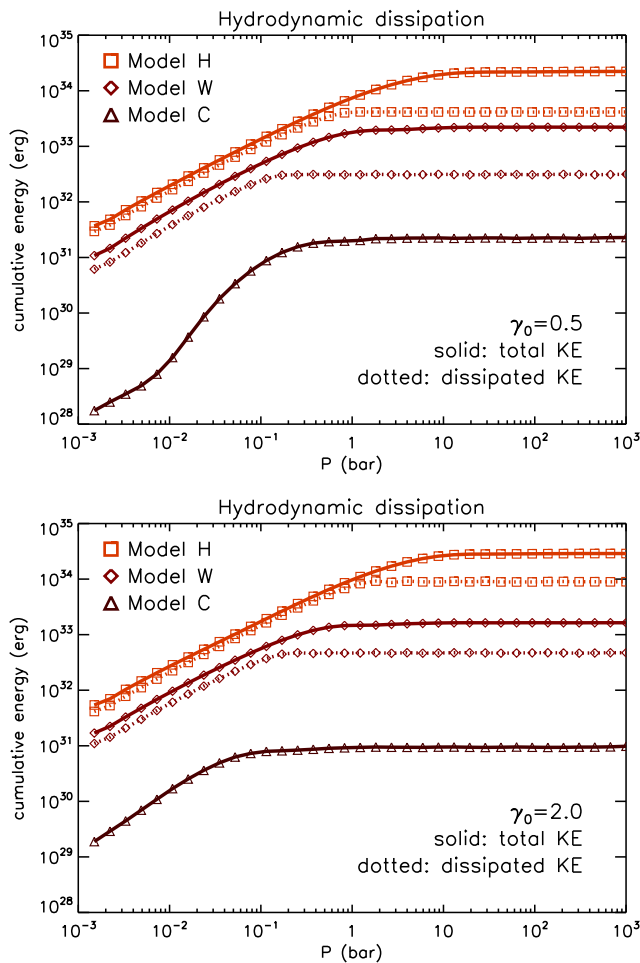


FIG. 5.— *Top*: Kinetic energy available within the flow, together with the amount available for dissipation through shear instabilities and shocks, for the three representative models C, W, H and no temperature inversions. *Bottom*: Same as above, but for the C, W, H models with temperature inversions.

We computed the Richardson number at each point of the flow. For Model C, we find $Ri > 1/4$ everywhere, and hence shear instabilities are not expected at low levels of irradiation. In the warm and hot models, we find $Ri < 1/4$ only in the outermost pressure levels, down to a few millibars. Hence, we conclude from this analysis that the onset and consequent dissipation of shear instabilities is unlikely to play a major role in inflating hot Jupiters.

4.1.2. Dissipation from shocked gas

In order to estimate the presence and amount of dissipation due to shocked gas, we begin by keeping track of the Mach number at each location within the flow; since zonal velocities are the most significant ones, we define the Mach number as

$$\mathcal{M}(\Theta, \Phi, r) = \frac{v_{\Theta}}{c_s}. \quad (16)$$

Shocks are likely to occur for $\mathcal{M} \gtrsim 1$, barring special conditions which allow the pre- and post-shock regions to remain in causal contact (Zel'dovich & Raizer 1966). One may regard our simple estimates of the shock dissipation as upper limits since $\mathcal{M} \gtrsim 1$ is a necessary but insufficient condition for the development of shocks.

At each pressure level within the atmosphere, flow velocities change with both latitude and longitude. To investigate how deep shocks can penetrate, in Fig. 4 we show the maximum Mach number as a function of atmospheric depth, for the three representative models C, W, and H, each with and without temperature inversions. In the coldest model, the flow is always subsonic. Wind speeds increase, as expected, with the strength of the irradiating flux and hence with the day-night temperature gradients. In the W model, the flow can become supersonic (with Mach numbers of $\sim 1.5 - 2$) at pressure levels above a few tens of bars. In the H model, shock penetration reaches a few bars, with Mach numbers $\sim 2.5 - 3$. For the same strength of irradiation, flows with temperature inversions reach a higher Mach number, due to the higher temperatures attained in the outermost layers.

In order to make a crude estimate of the amount of energy available to be dissipated in shocks, we first compute the total amount of kinetic energy available in the flow up to pressure P , $E_{\text{kin}}(P) = (1/2) \int_{r(P_0)}^{r(P)} dV \rho (v_{\Theta}^2 + v_{\Phi}^2)$. Note that the dominant term comes from the zonal component (v_{Θ}). Figure 5 shows $E_{\text{kin}}(P)$ in the three representative models C, W and H. The cumulative amount from the whole flow varies by over three orders of magnitude between the C and the H model, with a weaker dependence on the shortwave opacity. Generally, we find that the stronger the irradiation, the deeper the penetration of the zonal winds.

Together with the local kinetic energy density, we track, at each point of the flow, both the Mach number and the Richardson number. If either $\mathcal{M} > 1$ or $Ri < 1/4$, we assume that a fraction of 0.5 of the kinetic energy is dissipated/converted into heat. In strong shocks, this fraction is given by $4(\gamma - 1)/(\gamma + 1)^2$, where γ is the adiabatic index (Draine & McKee 1993); for $\gamma = 7/3$, this amounts to 0.48. For shear instabilities, Li & Goodman (2009) estimate the dissipated fraction of kinetic energy to be $\approx 0.5 - 1$. Hence we take $E_{\text{dis}}(P) = (1/2) f_{\text{dis}} \int_{r(P_0)}^{r(P)} dV \rho (v_{\Theta}^2 + v_{\Phi}^2)$, where $f_{\text{dis}} = 0.5$

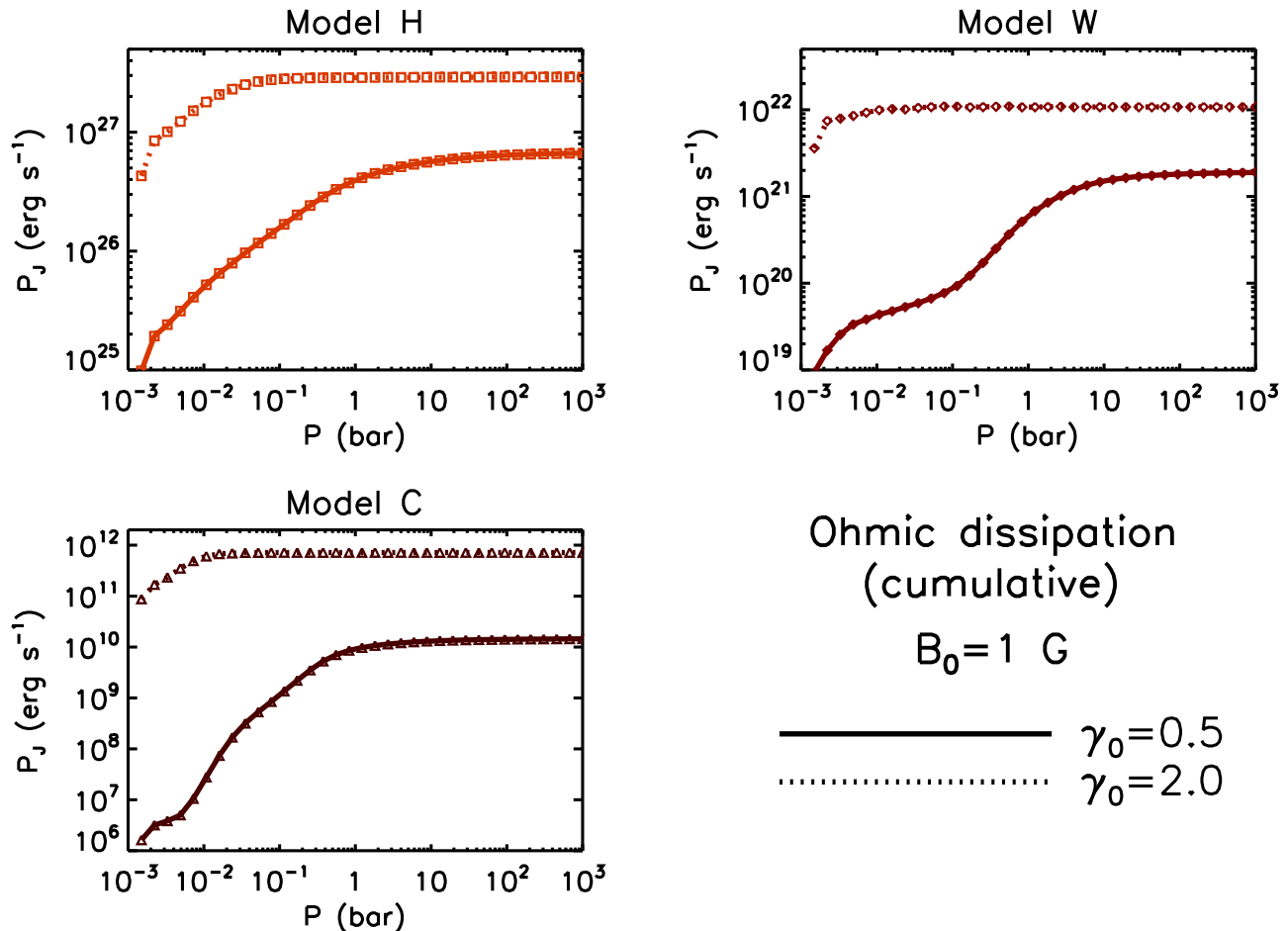


FIG. 6.— Dissipated Ohmic power as a function of depth, for the three representative models C, W, H, both with and without temperature inversions. A magnetic field strength of 2 G at the poles has been assumed. Note that the penetration depth increases with the strength of the irradiating flux; for the same T_{irr} , it is larger in models without temperature inversions.

if $\mathcal{M} > 1$ or $\mathcal{R}i < 1/4$ and $f_{\text{dis}} = 0$ otherwise. We remark once again that this is a rather crude estimate, motivated by the fact that current global 3D circulation models are not yet able to follow the development, growth, and dissipation of instabilities and shocks.

The cumulative dissipated energy, $E_{\text{dis}}(P)$, is shown in Fig. 5 for the C, W and H models. In the C model, $E_{\text{dis}}(P) = 0$ since, as discussed above, the criterion for the onset of the KH instability is never satisfied, and the velocities are always subsonic. In the W and H models, on the other hand, a fraction of about 10-20% of the kinetic energy is available for dissipation, with the fraction being generally larger in models with temperature inversions, due to the stronger velocities (and their gradients) in the upper atmospheric layers, which are the ones more prone to becoming either KH unstable or shocked. For a given value of γ_0 , dissipation occurs down to deeper levels as the strength of the irradiating flux increases, reflecting the penetration depth of the shocks (cf. Fig. 4). However, even in the hottest models, shock dissipation never penetrates deeper than a few bars.

4.2. Ohmic dissipation

Previous work (Batygin et al. 2010; Perna et al. 2010b) has shown that, for Jupiter-like magnetic field strengths, Ohmic dissipation can be a significant source

of energy for the exoplanet. In particular, using a simulation specialized to the physical parameters and conditions of HD 209458b, Perna et al. (2010b) showed that Ohmic dissipation can penetrate down to levels deep enough to influence the radius evolution of the exoplanet. Since irradiation is the driver of the flow dynamics, currents (and hence Ohmic dissipation) are expected to depend sensitively on its strength. In the following, we investigate this dependence using our 16 baseline models. We assume the B -field to be an axisymmetric dipole where the rotational and dipolar axes are aligned. The dependence of Ohmic dissipation on the magnitude of the B -field has been explored (inclusive of an approximate feedback from magnetic drag), by Perna et al. (2010b).

To compute Ohmic dissipation within the context of our simulations, we follow the formalism of Liu et al. (2008) and Perna et al. (2010b). Under the assumption that zonal winds are stronger than the meridional motions, the only relevant component of the induction equation is the toroidal one. Under steady-state conditions, it was showed by Liu et al. (2008) that the resulting dominant component of the current induced by the zonal flow is the meridional one, which we write below in terms of the latitude Φ and the longitude Θ , and also incorporating the expression for an aligned dipole for the

magnetic field:

$$\mathcal{J}_\Phi = \frac{B_0 r_{\max}^3 \sigma_e}{(r_{\max} - \tilde{z}) c} \int_0^{\tilde{z}} dz' \left[\frac{2 \sin \Theta}{(r_{\max} - z')^2} \frac{\partial v_\Theta}{\partial z'} + \frac{2 v_\Theta \sin \Phi}{(r_{\max} - z')^3} + \frac{\cos \Phi}{(r_{\max} - z')^3} \frac{\partial v_\Theta}{\partial \Phi} + \frac{v_\Theta \sin \Phi}{(r_{\max} - z')^3} \right]. \quad (17)$$

Here, $\eta = c^2/(4\pi\sigma_e)$ is the electrical resistivity, and the electrical conductivity σ_e is computed using the same formalism as in Perna et al. (2010a,b). The familiar radial coordinate, denoted by r , is equal to $z + R_p$ where z is the vertical height measured from the bottom of the simulation domain. The top of the simulation domain is located at $r_{\max} = \max(z + R_p)$. We choose to compute the current density as a function of the variable \tilde{z} , which is defined such that $\tilde{z} = 0$ when $r = r_{\max}$, i.e., it is the vertical height measured from the top of the model atmosphere. Again, v_Θ is the zonal velocity. The quantity B_0 is the normalization term in the dipole magnetic field, such that it is B_0 at the equator and $2B_0$ at the poles. For our calculations, we choose $B_0 = 1$ G. Note that in the above equation we have neglected the contribution from an unknown boundary current.

The total Ohmic power dissipated between the bottom shell at pressure P_0 and a shell of material located at pressure P , is then readily computed as

$$P_J(P) = \int_{r(P)}^{r(P_0)} dr' r'^2 \int_0^{2\pi} d\Theta \int_{-\frac{\pi}{2}}^{\frac{\pi}{2}} d\Phi \cos \Phi \frac{[\mathcal{J}_\Phi(r', \Theta, \Phi)]^2}{\sigma_e(r', \Theta, \Phi)}. \quad (18)$$

Fig. 6 shows the cumulative Ohmic power as a function of the atmospheric depth, for the three representative models C, W and H, both with and without temperature inversions. The magnitude of P_J has a very strong dependence on the irradiating flux, varying at maximum by about 16–17 orders of magnitude between the C and the H models. While the increasing zonal wind speeds with T_{irr} do contribute to this effect, the dominant factor is the exponential dependence of the electrical conductivity on temperature.

For the same T_{irr} , the maximum Ohmic power is larger for $\gamma_0 = 2$ (with a temperature inversion) than it is for $\gamma_0 = 0.5$ (no inversion), while the penetration depth on the other hand is larger for $\gamma_0 = 0.5$. This behaviour can be understood as follows. For $\gamma_0 = 2$, the outer layers of the atmosphere are hotter than the inner layers, and hence the conductivity is much larger in the outer atmospheric regions. Since velocity gradients are also stronger in these regions, the net result is the generation of very large peripheral currents and hence large dissipation, which however saturates, even in the hottest models, close to the photosphere. For $\gamma = 0.5$ on the other hand, the outer layers are colder, and the low conductivity results in weak currents. Deeper in, the temperature rises, and so does the conductivity, resulting in an increase of the Ohmic power at deeper atmospheric levels. However, the maximum dissipated power saturates at smaller values than than for the case of $\gamma_0 = 2$, since for $\gamma_0 = 0.5$ the region with higher conductivity corresponds to zonal flows with weaker gradients.

A comparison between the total power (i.e., integrated

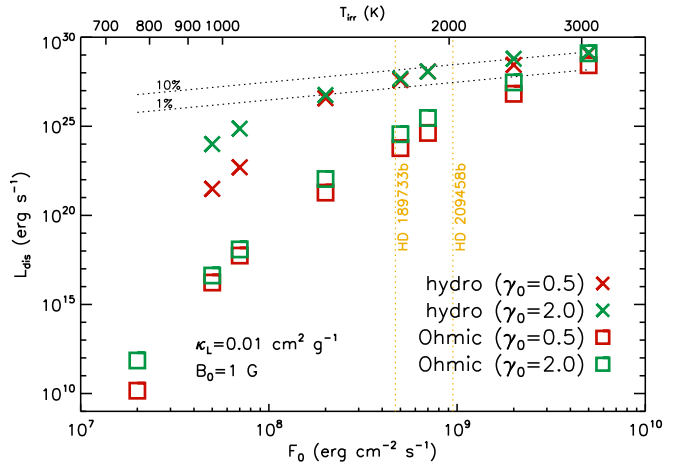


FIG. 7.— Comparison between hydrodynamic and Ohmic dissipation, for all of the models presented in our study. For the hydrodynamic dissipation, we assume that the energy is dissipated over a rotational timescale. The Ohmic power is computed for a dipolar B -field with strength of 2 G at the pole. Without feedback from magnetic drag, the Ohmic power scales as B_0^2 . The dotted lines labelled “1%” and “10%” correspond to 1% and 10% of the stellar irradiation, respectively.

over the entire atmosphere) generated through shocks and shear instabilities, and through Ohmic dissipation, is shown in Fig. 7. Since our simulations do not explicitly follow shocks and the development of shear instabilities, they cannot make predictions for the timescales over which dissipation associated with these phenomena occur. To compute the hydrodynamic power in Fig. 7, we assumed that E_{dis} is dissipated over a rotational timescale (which is comparable in magnitude to the advection timescale). The 2D simulations by Li & Goodman (2010) show that, once shocks are formed, they slow down over a very short time (shorter than the advection time). As long as the dissipation timescale is shorter than $2\pi/\Omega_p$, the power shown in Fig. 7 can be considered as a good proxy for its corresponding time-averaged quantity over a rotational cycle⁷.

Our simulations show that the Ohmic power is a much steeper function of irradiation than the hydrodynamic power, which we find to be dominated by shocks. For the latter, only velocities matter, while the dissipated Ohmic power depends on velocity gradients. But most importantly, as the temperature increases, so does the ionization fraction, and hence the conductivity, which results in stronger currents. However, we remark, once again, that the slope at high T_{irr} would be shallower if magnetic drag were included self-consistently in the simulations. Specifically, Menou (2012b) has shown, via simple scaling laws, that magnetic drag rapidly retards the atmospheric winds for strong stellar irradiation, and that, for a given magnetic field strength, there is a value of the irradiation/equilibrium temperature for which Ohmic dissipation peaks (and then declines as irradiation becomes more intense). Our results for the

⁷ Lacking 3D evolutionary planet models which can assess the effect of anisotropic heat injection in the planet interior on the thermal evolution of the planet, for an order-of-magnitude comparison with the 1D evolutionary models of Guillot & Showman (2002), we consider the averaged dissipated hydrodynamic power over a rotational cycle.

dissipated power should therefore be considered as upper limits.

Finally, we note that Heng (2012) provides a companion study to our paper by using semi-analytical models to elucidate the interplay between atmospheric scattering, absorption and Ohmic dissipation with relevance to the possible presence of atmospheric clouds or hazes.

4.3. Implications for the problem of radius inflation

As discussed in §1, the anomalously large radii of a fraction of hot Jupiters remains a persistent problem for researchers. An “extra” source of internal energy is needed for the radii to be larger than predicted by standard evolutionary models. Guillot & Showman (2002) argue that, if about 1% of the stellar insolation flux were deposited at pressures of tens of bars deep in the atmosphere, cooling would slow down sufficiently to explain the inflated radii of hot Jupiters. The evolutionary model presented by Guillot & Showman (2002) was tailored to the specific case of the exoplanet HD 209458b, with a radius of $R = 1.35R_J$ (R_J is the Jupiter radius), and a convective-radiative boundary located at pressures of about 1 kbar (at its current age). Note that, for exoplanets with comparable mass, the boundary layer between the convective/radiative zones is located at lower pressures as the planet is younger and larger (e.g., Guillot & Showman 2002, Burrows et al. 2003). The amount of internal heat needed to inflate the radius by a certain ΔR is also a strong function of the planet mass (Miller, Fortney & Jackson 2009). The smaller the mass, the easier it is to inflate the planet. For example, Miller et al. (2009) show that a 20% increase in radius (with respect to R_J) can be achieved with a mere 10^{24} erg s⁻¹ in a planet of mass $0.1 M_J$, while the same radius increment would require about 10^{28} erg s⁻¹ for a $10 M_J$ planet.

While several mechanisms could transport and dissipate energy into the interior, such as eccentricity damping (Bodenheimer et al. 2001), or forced turbulent mixing in the radiative layer (Youdin & Mitchell 2010), here we have investigated energy deposition resulting from the development of shear instabilities and shocks, and from Ohmic dissipation. For all of these phenomena, our numerical simulations, while not modeling the dissipation itself and its feedback on the flow, do allow us to estimate their importance from an energetic point of view, as a function of the strength of the irradiating flux and of the atmospheric opacity.

We have found that shear instabilities can develop only very superficially, even in the hottest models, and hence they are unlikely to meaningfully influence the energy budget of the exoplanet. If the source of weak turbulence postulated by Youdin & Mitchell (2010) results from shear instabilities, then their proposed mechanism of forced turbulent mixing does not operate deeply enough. To further test the relevance of their mechanism in global circulation models requires the specification of an instability and its criterion for being invoked.

Shocks penetrate deeper, up to a few bars in the hottest models. This is a depth which could be interesting for influencing the thermal evolution of planets, and hence the degree by which their radius is able to shrink during the evolution. For the particular case of HD 209458b, the evolutionary models of Guillot & Showman (2002) showed that, even at a pressure as shallow as 5 bars,

dissipation of 10% of the absorbed stellar flux (corresponding to $\dot{E} = 2.4 \times 10^{28}$ erg s⁻¹ for this planet) is sufficient to retard cooling so that the planet contracts to its current size on a timescale ~ 5 Gyr, comparable to its age. Inspection of the trend for the dissipated hydrodynamic power versus irradiating flux in Fig. 7, shows that, for the strength of \mathcal{F}_0 corresponding to the case of HD 209458b, the hydrodynamic power is on the order of a few $\times 10^{28}$ erg s⁻¹. Therefore, since the dissipated hydrodynamic power that our models predict falls in an interesting order of magnitude range (at least for the most irradiated objects), and its penetration depth also reaches levels close to the interesting ones identified by evolutionary models⁸, we suggest that shock dissipation could indeed play a significant role in the thermal evolution of the planets, and hence influence their radii, although especially so in the most irradiated planets.

Our investigation of Ohmic dissipation has showed that, for a B -field strength on the order of a Gauss, the total dissipated Ohmic power is generally lower than the hydrodynamic power except for the most irradiated hot Jupiters. However, it penetrates deeper, down to pressures of several tens of bars, if the atmosphere has no temperature inversion. In the evolutionary scenario of Guillot & Showman (2002), a deeper penetration depth can be “traded” for a smaller power. For example, in the case of HD 209458b, their evolutionary models could reproduce the exoplanetary radius at its current age both with 10% of the irradiating flux dissipated at 5 bars, or with 1% (i.e., 2.4×10^{27} erg s⁻¹) dissipated at 21 bars. For a B -field strength of a few Gauss, this power is available in the most irradiated objects. Clearly, the importance of Ohmic dissipation for the thermal evolution of planets also depends strongly on the magnitude of the B -field, since the Ohmic power scales as⁹ B_0^2 , and, for fixed planet conditions, the penetration depth also increases with larger B_0 (Perna et al. 2010b). However, for a given B -field, since both the penetration depth and the power dissipated at a fixed pressure are rapidly increasing functions of the strength of the irradiating flux, the influence of Ohmic dissipation on radius inflation is expected to depend strongly on stellar irradiation.

5. QUALITATIVE COMPARISON WITH OBSERVATIONS

Observations of hot Jupiters have allowed to characterize, albeit with varying statistical level, the atmospheric properties that we have discussed so far, and in particular, the efficiency of heat redistribution, the hotspot offset and the exoplanetary radius. Here we do not attempt to make any detailed, quantitative comparison between our models and the data; the former have been constructed for “typical” values of the exoplanetary parameters, and hence they are not generally applicable to a specific object. For the same value of the irradiating

⁸ It is also important to note that vertical advection can help transport the dissipated energy to deeper levels. In our models, the vertical advection timescale is $\sim 10^5$ s, comparable to the advection timescale; for an HD 209458b-like planet, Heng, Frierson & Phillipps (2011) showed that vertical mixing extends down to about 10 bars.

⁹ As discussed in §4.2, this scaling would be shallower if feedback effects from magnetic drag were accounted for, but it would still remain an increasing function of B_0 for a wide range of irradiating fluxes.

flux, a scatter is expected due to the different intrinsic properties of the exoplanet, of which here we have only examined the dependence on the shortwave opacity for two values. (See Heng 2012 for a broader exploration of γ_0 values, and also the influence of shortwave scattering, using semi-analytical models.) The data on the other hand, still suffer from measurement uncertainties which would make quantitative comparisons with models not fully reliable yet. However, the *qualitative trends* in both the data and the model are fairly robust, and these are the ones that we are interested in reproducing at this stage.

5.1. Data summary

Figure 8 summarizes the main observational constraints on the radius inflation and atmospheric circulation of hot gas giant exoplanets. The exoplanetary radius measured for transiting gas giants ($M > 0.3M_J$) is shown as a function of the irradiation temperature. Different symbols indicate more/less massive exoplanets, exoplanets with or without a temperature inversion measured near the infrared photosphere, and exoplanets with or without efficient day-night temperature redistribution. The presence of a temperature inversion is inferred from the broadband infrared emission spectra measured during secondary eclipse with the *Spitzer* satellite. The efficiency of the day-night temperature redistribution is inferred from the comparison of the effective temperature in the *Spitzer* passbands with the equilibrium temperature. If the measured temperature is much larger than the equilibrium temperature, the redistribution of heat to the night side is likely to be low¹⁰. In one case, HD 189733b, the heat redistribution is measured more directly, from the infrared phase curve of the exoplanet at 8 and 24 microns (Knutson et al. 2007, 2009).

The exoplanet radii and irradiation data have been taken from the edited compilation at www.inscience.ch/transits (see references therein for primary sources). Information on the absence/presence of temperature inversions is adopted from Knutson et al. (2011, see references therein), while information on redistribution is taken from the compilation of Harrington (2011), updated with more recent data from *Spitzer* for HD80606, XO-3, HAT-P-7 and WASP-12; we also include inferences on XO-4, HAT-P-6 and HAT-P-8 (Todorov et al. 2011). It is important to note that inferences on redistribution (presented in the lower panel of Figure 8) are based on data that stretches the capacity of the *Spitzer* instruments to their limits, and that the uncertainties associated with instrumental effects are still high. In at least two cases, Ups And b and HD 149026b, further measurements have shown the initial estimates for the surface temperature and redistribution efficiency to be completely incorrect. These two objects are not in our plot, Ups And b because it is not a transiting planet and therefore its radius is not measured, and HD 149026b because it is not in synchronous rotation and is a core-dominated

¹⁰ This inference is tentative, since the albedo and the redistribution of flux in frequency by molecular spectral features will also play a role. The indications for specific objects may turn out to be incorrect, but hopefully this will simply introduce some random noise and not entirely mask the existing correlations between the efficiency of redistribution and other parameters.

planet rather than a hot Jupiter, and therefore it does not fit our model assumptions.

Information on the angular offset of the hotspot is only sparsely available. *Spitzer* observations of HD 189733b show that the hottest region of the thermal phase curve is advected to the east of the substellar point (Knutson et al 2007) by 16 ± 6 degrees; Knutson et al. (2009) inferred the 1D brightness maps at 8 and 24 microns and found the offsets to be 30 ± 4 and 23 ± 7 degrees, respectively. Measurements for a couple of other objects are less certain. Crossfield et al. (2010) report, for Ups And b, which has a good redistribution, an offset of the 1D brightness map to the east of either 57 ± 21 degrees or 84.5 ± 2.3 degrees, using two different data sets for the analysis. Cowan et al. (2012), report, for WASP-12b, an offset to the east of 12 ± 6 degrees from the *Spitzer* phase curve at 4.5 microns, and an offset of 53 ± 7 degrees at 3.6 microns.

5.2. Observational vs. theoretical trends

Figure 8 illustrates the strong correlation between irradiation and radius inflation. This indication that injection of a fraction of the irradiation into the exoplanet as internal entropy is responsible for the radius inflation (as first suggested by Showman & Guillot 2002) is reinforced by the observed correlation between radius inflation and the mass of the exoplanet (Fortney et al. 2011), and by the absence of radius inflation for cooler Jupiter-sized exoplanet candidates from the Kepler mission (Demory & Seager 2011). Hence, the observations strongly support explanations of radius inflation as a consequence of high stellar irradiation. The observed slope of the dependence, though, seems even steeper than that predicted by the injection of a constant fraction of the stellar flux as internal entropy as proposed by Showman & Guillot (2002), suggesting that the efficiency of the coupling mechanism increases with temperature. There is no significant correlation between radius inflation and orbital eccentricity (Pont 2009), nor with temperature inversion.

For the dissipation mechanisms that we have explored in this work, both of hydrodynamic and of magnetohydrodynamic origin, our simulations show a strong correlation with the strength of the irradiating flux. In particular, for a B -field on the order of a Gauss, we found that, for $T_{\text{irr}} \lesssim 2000$ K, the dissipated Ohmic power is too small (and its penetration depth too shallow), to affect the radius evolution in any appreciable way. However, as T_{irr} approaches ~ 2000 K, the Ohmic power grows noticeably, and its penetration depth, reaching down to several tens of bars, can then affect the evolution of the exoplanetary radius (Guillot & Showman 2002). Interestingly, as Fig. 8 shows, radius inflation starts to become important as the irradiation temperature approaches the 2000 K range. We also note that variations of the magnetic field from exoplanet to exoplanet can result in a substantial scatter in the radius evolution, since the Ohmic power scales as B_0^2 , and this rapid growth with magnetic field strength dominates over the reduction to the power caused by the feedback effect of magnetic drag, at least for an interesting range of B -field strengths (Perna et al. 2010b). For a Jupiter-like magnetic field (~ 14 G at the pole), the power produced by Ohmic dissipation can already affect planets with $T_{\text{irr}} \sim 1700 - 1800$ K. The atmospheric (shortwave) opacity further contributes to the

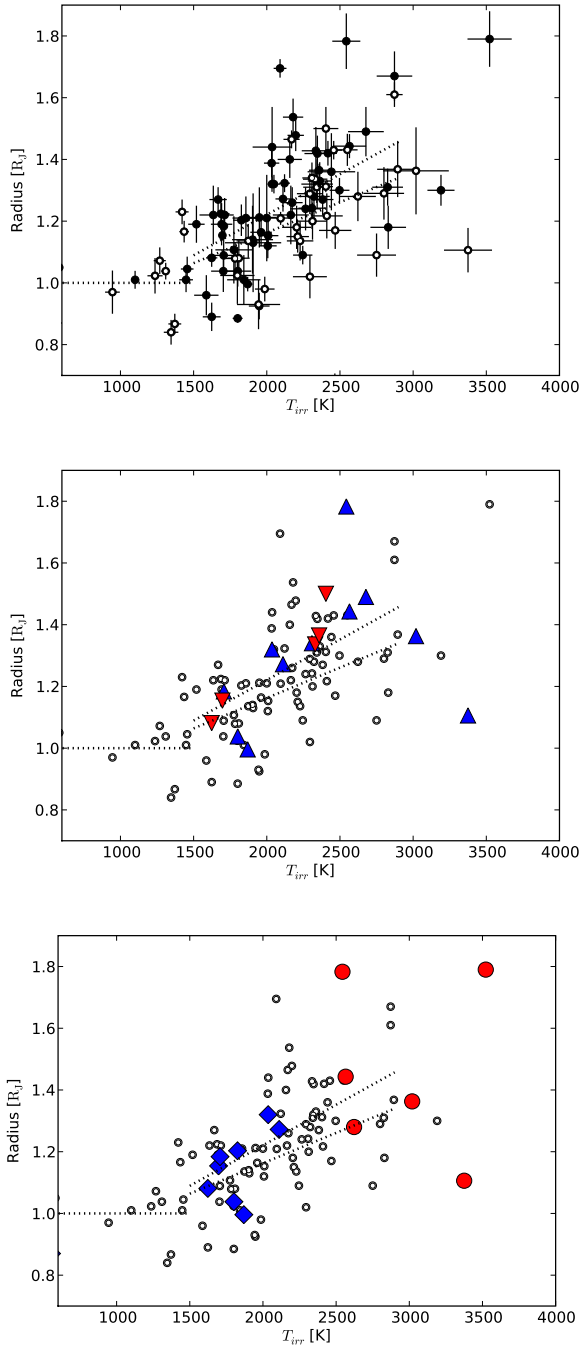


FIG. 8.— *Upper panel:* Exoplanetary radius as a function of irradiation temperature for transiting gas giants. Exoplanets in the range $0.3 < M < 1.5M_J$ are shown as closed symbols, exoplanets heavier than $1.5M_J$ as open symbols (data from www.inscience.ch/transits). Dotted lines show the temperature range where no significant radius anomaly is observed (flat line), and least-square linear fits to the low-mass data and high-mass data separately. *Middle panel:* Same data as in the upper panel, but with upside-down red triangles indicating inverted temperature profiles, and blue triangles normal profiles. *Bottom panel:* Same data as in the other two panels, but with blue diamonds indicating probable efficient redistribution, and red circles probable strong day-night contrast.

scatter, since the penetration depth of Ohmic dissipation is a non-negligible function of this variable.

In summary, and at a qualitative level, our simulations predict that both hydrodynamic dissipation (dominated by shocks) and Ohmic dissipation (for magnetic field strengths at least as large as several Gauss), can play an important role in altering the thermal evolution of hot Jupiters, slowing down cooling, and favoring the presence of planets of larger dimensions than predicted by evolutionary models without “extra” energy injection. A significant dissipated power (both hydrodynamic and Ohmic if $B_0 \gtrsim 7 - 8$ G), on the order of several percents of the stellar insolation, is predicted for irradiation temperatures $T_{\text{irr}} \gtrsim 1700 - 1800$ K. For both forms of dissipation, the stronger the irradiating flux, the larger the total dissipated power and the deeper the penetration depth, resulting in an increasingly larger inflation as the flux becomes more intense. At large insolation, even if the direct dissipation depth is rather shallow (as it is for shocks and for currents in highly inverted temperature profiles), vertical mixing can help to carry down heat to levels of tens of bars, hence maintaining the energy injection in the relevant regions for affecting the thermal evolution of the planet.

A quantitative prediction of the slope of the $R_p(T_{\text{irr}})$ curve would need a coupling between a specific dissipation mechanism and an evolutionary model for the exoplanet, which is beyond the scope of the present study. But even so, as discussed above, a large scatter would be expected due to exoplanets with different intrinsic properties (opacity, gravity, magnetic field strength, etc).

Although the statistical information is still rather limited, inspection of Fig. 8 further shows that the efficiency of day-night heat redistribution seems to diminish rapidly for T_{irr} above 2200 K, with the hottest gas giants showing day-side temperatures in the infrared much higher than the equilibrium temperature, an effect pointed out by Harrington (2011). Interestingly, our simulations (cf. Fig. 2) also show that, from irradiation temperatures around 2200–2500 K, the atmospheric flow pattern begins to evolve from a very good redistribution to a regime of no-redistribution. Exoplanets with temperature inversions evolve more quickly towards a no-redistribution regime by displaying, for the same irradiating flux, a larger day-night flux contrast. This is again supported by observations, as well as by other work (Fortney et al. 2008). It may also be worthwhile to note that the drop in redistribution efficiency appears to occur around the temperature at which radius inflation saturates, although this is only a tentative indication at this point due to the low number of known cases, the large scatter at high temperatures, and the assumptions involved in inferring redistribution from infrared day-side fluxes in the *Spitzer* passbands. From a theoretical point of view, a saturation of radius growth at very high values of T_{irr} is expected due to feedback effects (e.g., shock dissipation and magnetic drag, both contributing to reduce the speeds of the fastest flows).

For the hotspot offset with respect to the substellar point, there is insufficient data statistics yet to compare theoretical and observational trends. However, we do note that, as the observations show that the offset can be both rather small or very large, our theoretical modeling also shows a wide range of values, and further predicts a

correlation between offset width and degree of redistribution. Although our modeling here has been for “typical” exoplanets and is not tailored to the properties of specific objects, it is however tempting to point out that, with the irradiating flux level of HD 189733b, our predicted offset is in the 20° – 40° range (cf. Fig. 3), consistent with the range of values (16° – 34°) obtained from the inferred 1D brightness maps, at 8 and 24 microns, by Knutson et al. (2009). In the case of Wasp-12b, the extremely high value of the irradiation temperature, $T_{\text{irr}} \sim 3500$ K, is above the temperature range studied in our simulations. However, inspection of the offset trend at high T_{irr} in Fig. 3 would suggest a value around a couple of tens of degrees at those high temperatures. The measured offset of 16 ± 4 degrees at 4.5 microns appears compatible with this estimate. On the other hand, the much larger offset of 53 ± 7 degrees at 3.6 microns does not. The difficulty in reconciling this large phase offset with the other properties of the object was already discussed by Cowan et al. (2012), though they also noted that the measurement could be affected by highly-correlated residuals near the purported peak. If real, such a measurement might indicate a rather unusual opacity, and a detailed theoretical modeling would require a non-grey radiative transfer treatment (Fortney et al. 2006, Showman et al. 2009, Burrows et al. 2010). Similarly, for the case of Ups And b, the unusually large offset values reported by Crossfield et al. (2010), albeit with somewhat large error bars, cannot be simply accounted for with the opacity values adopted here. However we note that, even within the simple framework of the dual-band model, larger offsets can be produced for smaller values of both the optical and infrared opacities.

6. SUMMARY

Irradiation by the parent star is the main driver of the radiative and dynamical properties of hot Jupiters. Opacity in the exoplanetary atmosphere further plays an important role in determining the response of the atmospheric flow to a certain amount of irradiating flux.

In this paper, by means of 3D atmospheric circulation models with dual-band radiative transfer, we have explored the role of irradiation and opacity in determining some of the main observational properties of hot gaseous exoplanets, with particular emphasis on heat redistribution and on hydrodynamic and magnetohydrodynamic dissipation. Although our simulations are still idealized in several respects (simplified radiative transfer, constant opacities, lack of feedback effects due to dissipation of instabilities and shocks and to magnetic drag), they still allow us to capture some broad trends exhibited by the observations.

Our results are summarized below:

- For irradiation temperatures $T_{\text{irr}} \lesssim 2200 - 2400$ K, we find heat redistribution to be very efficient. Near-perfect redistribution (i.e., $F_{\text{day}}/F_{\text{night}} \approx 1$) only occurs up to $T_{\text{irr}} \lesssim 1500$ K, but in the range $1500 \text{ K} \lesssim T_{\text{irr}} \lesssim 2400 \text{ K}$ the day-night flux contrast is still relatively small ($\lesssim 2$). As the stellar irradiation becomes more intense, redistribution begins to fail. Observations, albeit limited by the low statistics, hint at the redistribution breaking down around $T_{\text{irr}} \gtrsim 2200 - 2400$ K, in broad agree-

ment with our theoretical results. Our simulations support the simple intuitive result that it is the interplay between advection and radiative cooling which determines the effectiveness of heat redistribution. Redistribution begins to falter as the advective timescale becomes much longer than the radiative timescale.

- For the same strength of irradiation, exoplanets with a temperature inversion (here parameterized by means of a larger shortwave opacity) display a higher day-night contrast than exoplanets with no temperature inversion, since starlight is deposited higher up in the layers of the atmosphere dominated by radiative cooling (rather than advection).
- The offset of the hottest region (hotspot) from the substellar point can exhibit a wide range of values; it is generally very large (even entering the night side) for exoplanets with very efficient redistribution (low T_{irr}) and it moves closer to the substellar point with increasing strength of the irradiating flux. For a fixed value of the irradiating flux, opacity further plays a role in determining the offset. The smaller the shortwave opacity, the larger the offset for the same T_{irr} .
- A measurement of the Richardson number throughout the 3D flow showed that the Kelvin-Helmholtz instability is unlikely to play a major role in the thermal evolution of the planet. We found that the criterion for the instability onset, $\mathcal{R}_i < 1/4$, is satisfied only in the uppermost layers of the flow, down to several millibars (if at all).
- Shocks, associated with the presence of supersonic flows (up to Mach numbers of $\sim 2.5 - 3$ in the hottest models), can dissipate up to 10-20% of the available kinetic energy. The total dissipated power over an advective timescale reaches several percent of the insolation energy power for irradiation temperatures $T_{\text{irr}} \gtrsim 1700 - 1800$ K, and it then increases with T_{irr} . Hence, for the most irradiated objects, the magnitude of the hydrodynamic power is such that it could noticeably influence the thermal evolution of planets. However, the direct penetration depth of the dissipation does not extend beyond a few bars even in the most irradiated hot Jupiters. Some amount of vertical advection would then be necessary to bring the heat to deeper levels. In the most irradiated objects, our simulations predict vertical mixing to penetrate down to tens of bars (see Appendix A), which could make hydrodynamic dissipation an interesting contributor to the thermal evolution of the exo-Jupiters, and hence affect the evolution of their radii.
- For a Jupiter-like B -field strength, Ohmic dissipation is negligible up to irradiation temperatures $T_{\text{irr}} \lesssim 1700 - 1800$ K, as far as the power needed to influence the thermal evolution of the hot Jupiters. As the insulating flux becomes stronger, the magnitude of the dissipation increases, and so does its penetration depth. The latter effect is however

much more pronounced in models without temperature inversions, which have a hotter interior. Dissipation can occur down to levels of several tens of bars, hence potentially affecting the radius evolution of the exoplanet. If Ohmic dissipation does play a major role in radius inflation, a strong correlation with the strength of the irradiating flux is naturally predicted. However, a large scatter is also expected, due to the strong dependence of the Ohmic power on the magnetic field strength, as well as on the atmospheric opacities.

This work was partially supported by grant NSF AST-

1009396 (RP), the Zwicky Prize Fellowship (KH) and the STFC Advanced Fellowship (FP). RP thanks the ETH for the wonderful hospitality during the time that some of this work was carried out. KH benefited from stimulating discussions conducted at the Exoclims II conference, held at the Aspen Center for Physics. We are grateful to Olivier Byrde and his team for supporting our use of the Brutus computing cluster at ETH Zürich, which served as the workhorse for our simulations. Finally, we thank the referee, Jonathan Fortney, for very useful comments on the manuscript.

APPENDIX

ZONAL WIND, TEMPERATURE, POTENTIAL TEMPERATURE AND STREAMFUNCTION PROFILES

For completeness, we include the temporally- and zonally-averaged zonal wind (Figure 9), temperature (Figure 10), potential temperature (Figure 11) and Eulerian mean streamfunction (Figure 12) profiles as functions of latitude and pressure/height. The contours of constant potential temperature are equivalent to contours of constant specific entropy. As already noted in Heng, Frierson & Phillipps (2011), computing the Eulerian mean streamfunction only on the dayside hemisphere strictly violates the definition of a streamfunction, but it does illustrate the nature of the global circulation pattern and the depth to which it penetrates.

REFERENCES

- Baraffe, I., Selsis, F., Chabrier, G., Barman, T. S., Allard, F., Hauschildt, P. H., Lammer, H. 2004, *A&A*, 419L, 13
- Batygin, K. & Stevenson, D. J. 2010, *ApJ*, 614L, 238
- Bodenheimer, Peter, Lin, D. N. C., Mardling, R. A. 2001, *ApJ*, 548, 466
- Burrows, A., Sudarsky, D., Hubbard, W. B. 2003, *ApJ*, 594, 545
- Burrows, A., Hubeny, I., Budaj, J., Hubbard, W. B. 2007a, *ApJ*, 661, 502
- Burrows, A., Hubeny, I., Budaj, J., Knutson, H. A., Charbonneau, D. 2007b, *ApJ*, 688L, 171
- Burrows, A., Orton, G. 2010, in *Exoplanets*, edited by S. Seager. Tucson, AZ: University of Arizona Press, 526, p.419-440
- Burrows, A., Rauscher, E., Spiegel, D. S., Menou, K. 2010, *ApJ*, 719, 341
- Burkert, A. Lin, D. N. C., Bodenheimer, P. H., Jones, C. A., Yorke, H. W. 2005, *ApJ*, 618, 512
- Cowan, N.B., & Agol, E. 2008, *ApJ*, 678, L129
- Cowan, N. B., Machalek, P., Croll, B., Shekhtman, L. M., Burrows, A., Deming, D., Greene, T., Hora, J. L. 2012, preprint (arXiv:1112.0574)
- Crossfield, I. J. M., Hansen, B. M. S., Harrington, J., Cho, J. Y.-K., Deming, D., Menou, K., Seager, S. 2010, *ApJ*, 723, 1436
- Demory, B.-O., & Seager, S. 2011, *ApJ*, in press (arXiv:1110.6180)
- Dobbs-Dixon, I., Cumming, A., & Lin, D.N.C. 2010, *ApJ*, 710, 1395
- Draine, B.T., & McKee, C.F. 1993, *ARA&A*, 31, 373
- Fortney, J. J., Cooper, C. S., Showman, A. P., Marley, M. S., Freedman, R. S. 2006, *ApJ*, 652, 746
- Fortney, J. J., Lodders, K., Marley, M. S., Freedman, R. S. 2008, 683, 1104
- Fortney, J. J. & Nettelmann, N. 2010, *Space Sc. Rev.*, 152, 423
- Fortney, J.J., et al. 2011, *ApJS*, 197, 9
- Goldreich, P., & Soter, S. 1966, *Icarus*, 5, 375
- Goody, R.M., & Yung, Y.L. 1989, *Atmospheric radiation: theoretical basis*, 2nd edition (New York: Oxford University Press)
- Guillot, T. & Showman, A. P. 2002, *A&A*, 385, 156
- Guillot, T. 2008, *Phys. Scripta*, 130a, 4023
- Harrington, J. 2011, EPSC-DPS Joint Meeting 2011, held 2-7 October 2011 in Nantes, France. <http://meetings.copernicus.org/epsc-dps2011>, vol. 6, p.1690
- Heng, K., Menou, K., & Phillipps, P.J. 2011, *MNRAS*, 413, 2380
- Heng, K., Frierson, D.M.W., & Phillipps, P.J. 2011, *MNRAS*, 418, 2669
- Heng, K., Hayek, W., Pont, F., & Sing, D.K. 2012, *MNRAS*, 420, 20
- Heng, K. 2012, 748, L17
- Hubeny, I., Burrows, A., Sudarsky, D. 2003, *ApJ*, 594, 1011
- Ibgui, L. & Burrows, A. 2009, 700, 1921
- Jackson, B. Greenberg, R., Barnes, R. 2008, *ApJ*, 681, 1631
- Knutson, H. A., Charbonneau, D., Allen, L. E., Fortney, J. J., Agol, E., Cowan, N. B., Showman, A. P., Cooper, C. S., Megeath, S. T. 2007, *Nat.*, 448, 143
- Knutson, H. A., Charbonneau, D., Allen, L. E., Burrows, A., Megeath, S. T. 2008, *ApJ*, 673, 526
- Knutson, H. A., Charbonneau, D., Cowan, N. B., Fortney, J. J., Showman, A. P., Agol, E., Henry, G. W., Everett, M. E., Allen, L. E. 2009, *ApJ*, 690, 822
- Knutson, H. A. et al. 2011, *ApJ*, 735, 27
- Kundu, P.K., & Cohen, I.M. 2004, *Fluid Dynamics*, third edition (San Diego: Elsevier)
- Lewis, N. K., Showman, A. P., Fortney, J. J., Marley, M. S., Freedman, R. S., Lodders, K. 2010, *ApJ*, 720, 344
- Li, J. & Goodman, J. 2010, *ApJ*, 725, 1146
- Liu, J., Goldreich, P. M., Stevenson, D. J. 2008, *Icar.*, 653, 664
- Menou, K. 2012a, *ApJ*, 744, L16
- Menou, K. 2012b, *ApJ*, in press (arXiv:1108.3592)
- Miller, N., Fortney, J. J., Jackson, B. 2009, *ApJ*, 702, 1413
- Perna, R., Menou, K., Rauscher, E. 2010a, *ApJ*, 719, 1421
- Perna, R., Menou, K., Rauscher, E. 2010b, *ApJ*, 724, 313
- Pierrehumbert, R.T. 2010, *Principles of Planetary Climate* (New York: Cambridge University Press)
- Pont, F. 2009, *MNRAS*, 396, 1789
- Rauscher, E. & Menou, K. 2012, preprint (arXiv:1112.1658)
- Showman, A.P., & Guillot, T. 2002, *A&A*, 385, 166
- Showman, A. P., Fortney, J. J., Lian, Y., Marley, M. S., Freedman, R. S., Knutson, H. A., Charbonneau, D. 2009, *ApJ*, 699, 546
- Youdin, A. N. & Mitchell, J. L. 2010, *ApJ*, 721, 1113
- Winn, J. N. & Holman, M. 2005, *ApJ*, 628L, 159
- Zel'dovich, Ya.B., & Raizer, Yu.P. 1966, "Physics of Shock Waves and High-Temperature Hydrodynamic Phenomena", Vols. 1 & 2, eds. W.D. Hayes & R.F. Probstein (New York: Dover Publications)

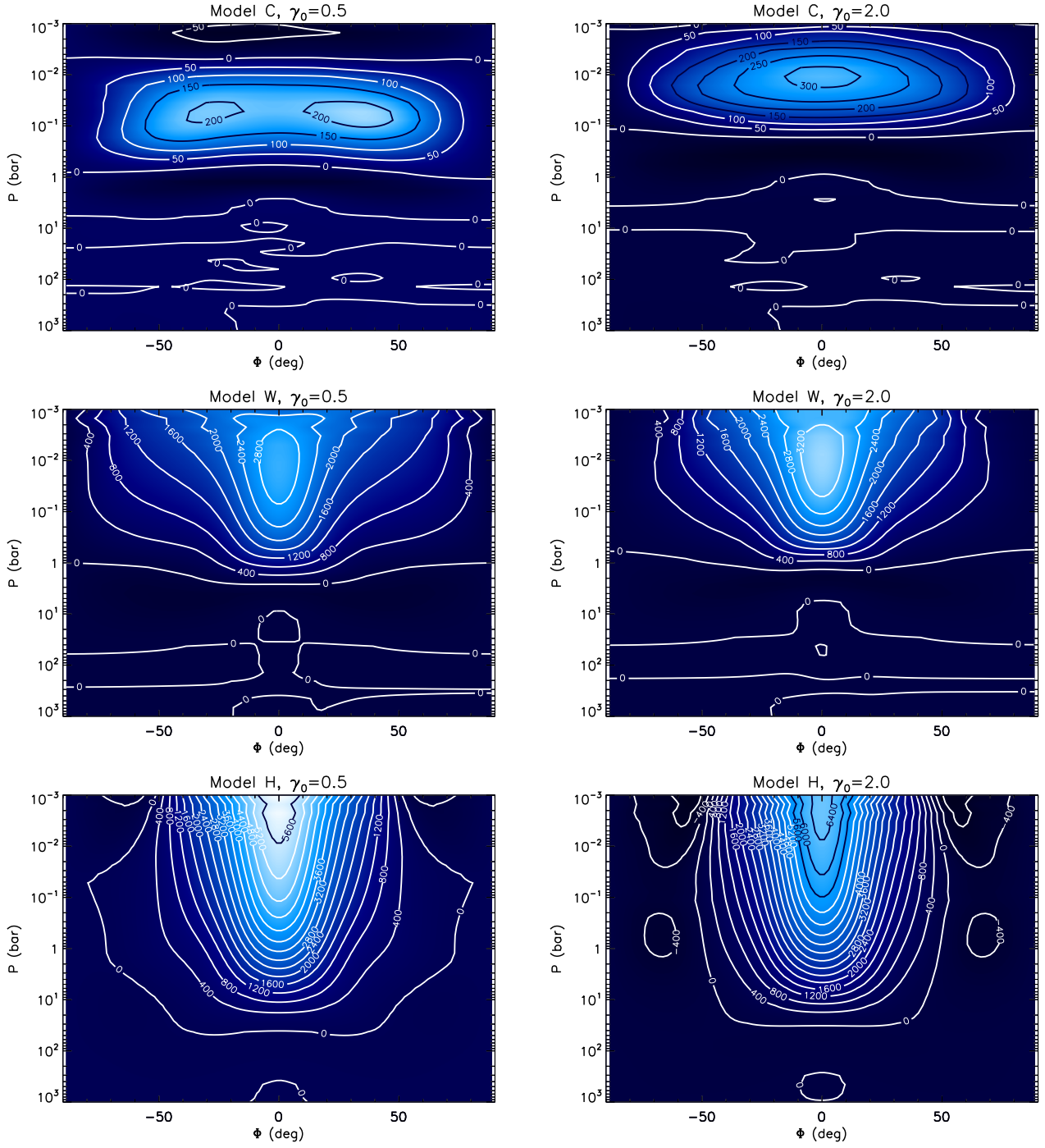


FIG. 9.— Temporally- and zonally-averaged zonal wind profiles for Models C, W and H and for $\gamma_0 = 0.5$ and 2. Contours are in units of m s^{-1} .

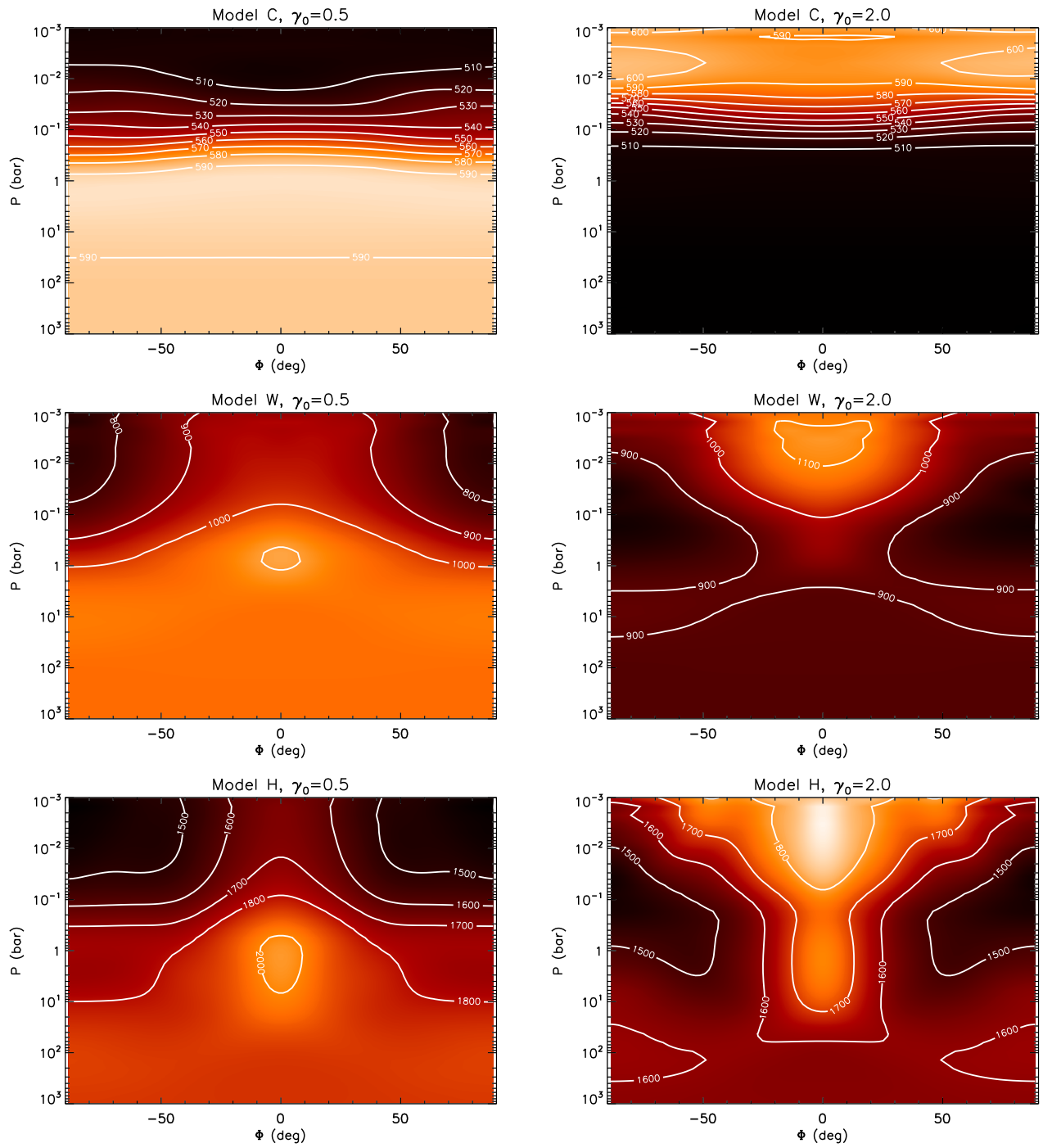


FIG. 10.— Same as Figure 9 but for the temporally- and zonally-averaged temperature profiles. Contours are in units of K.

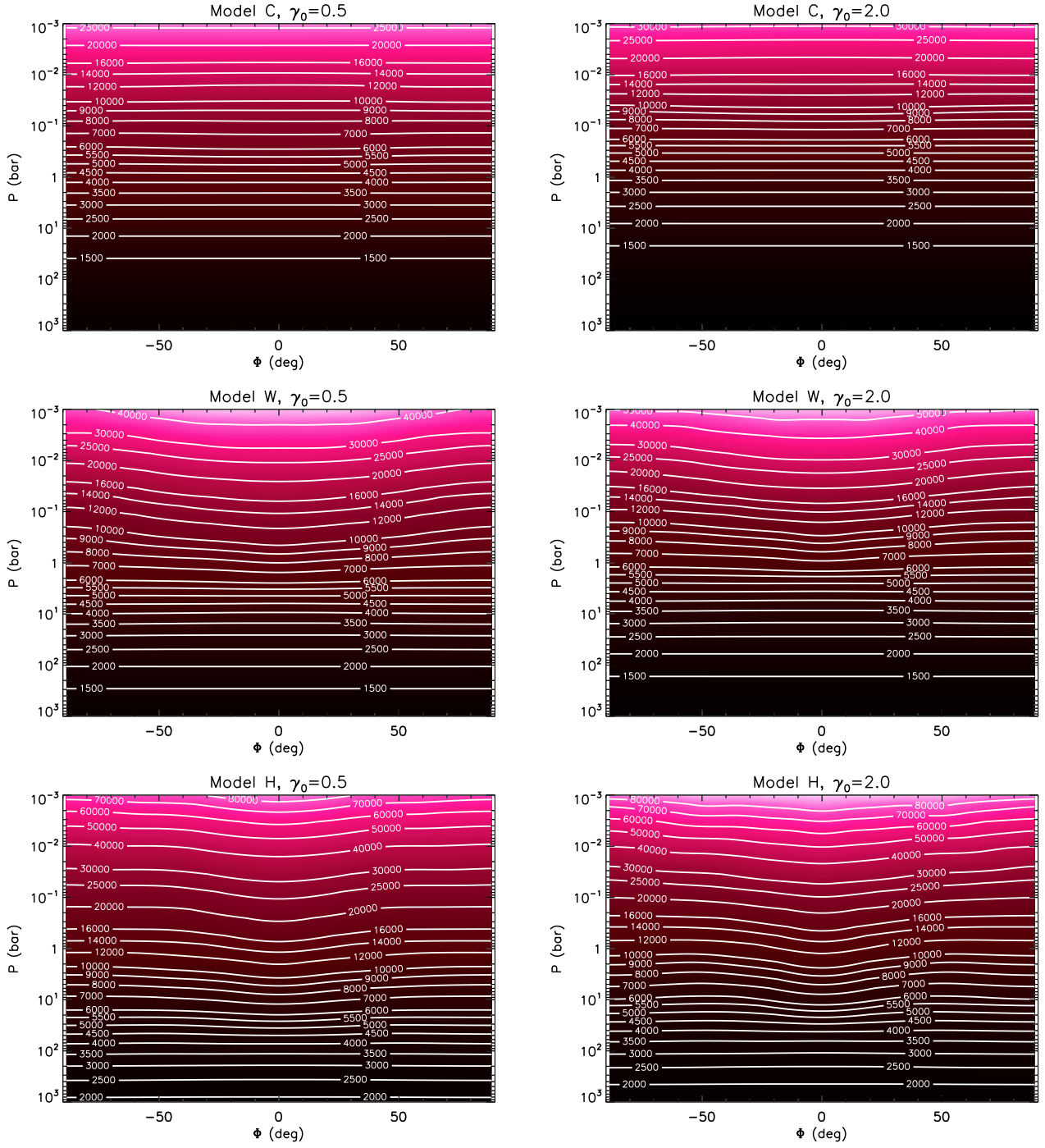


FIG. 11.— Same as Figure 9 but for the temporally- and zonally-averaged potential temperature profiles. Contours are in units of K. Lines of constant potential temperature are equivalent to lines of constant entropy (isentropes).

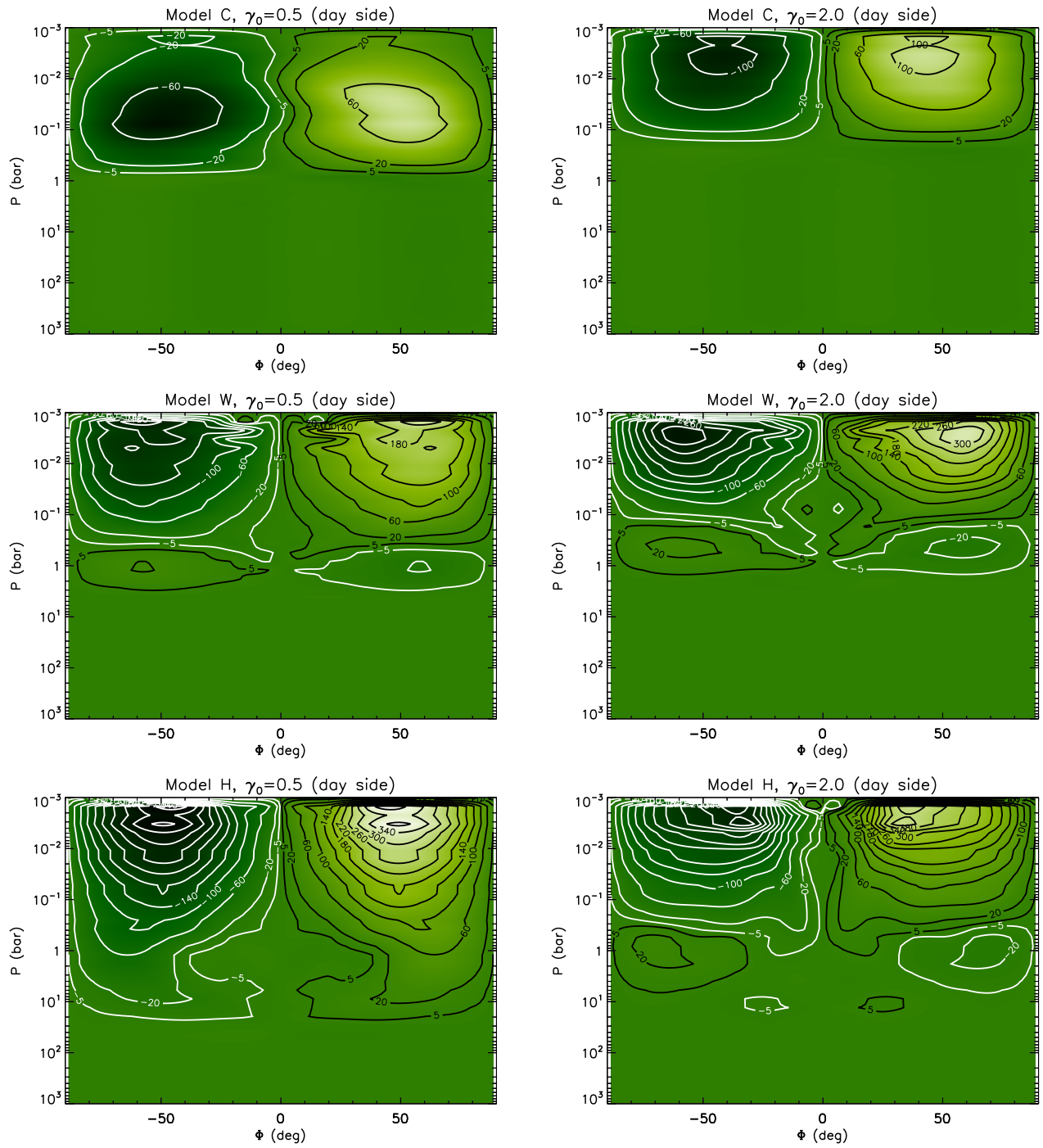


FIG. 12.— Same as Figure 9 but for the temporally- and zonally-averaged Eulerian streamfunction profiles only on the dayside hemisphere. Contours are in units of $10^{13} \text{ kg s}^{-1}$. Negative and positive values indicate clockwise and anti-clockwise circulation, respectively.